Published in final edited form as:
Mol Imaging. 2012 ; 11(5): 426–432.

[^{18}F]-2′-fluoro-5-methyl-1-beta-D-arabinofuranosyluracil (^{18}F-FMAU) in Prostate Cancer: Initial Preclinical Observations

Hossein Jadvar, MD, PhD, MPH, MBA, **Li-Peng Yap, PhD**, **Ryan Park, MS**, **Zibo Li, PhD**, **Kai Chen, PhD**, **Lindsey Hughes, MS**, and **Peter Conti, MD, PhD**
Molecular Imaging Center, Department of Radiology, Keck School of Medicine, University of Southern California, Los Angeles, CA, USA

Abstract

We hypothesized that imaging-based assessment of cellular proliferation in prostate cancer may improve tumor characterization. We therefore evaluated the biodistribution and effect of androgen on tumor uptake of the cellular proliferation imaging marker [^{18}F]-2′-fluoro-5-methyl-1-beta-D-arabinofuranosyluracil (^{18}F-FMAU) in xenograft mouse models of human prostate cancer. Castrated and noncastrated athymic male mice were implanted with androgen-independent PC3 and androgen-sensitive CWR22 human prostate cancer cells. Dynamic microPET/CT imaging was performed for 1h followed by 10 minute static scans at 2h and 3h. Animals were sacrificed after imaging for biodistribution studies and immunohistochemical staining of tumors for androgen receptor and Ki-67/MIB expression. ^{18}F-FMAU uptake was significantly higher in all major organs of the castrated animals in comparison to noncastrated mice with the highest uptake in liver and the lowest uptake in muscle and bone. When compared to PC3 tumors, CWR22 xenografts showed significantly higher tumor-to-muscle (2.56±0.30 vs. 1.99±0.30, p=0.008) and tumor-to-liver uptake ratios (1.72±0.12 vs. 1.26±0.17, p=0.0003) in the noncastrated animal at 3h time point. Androgen receptor and Ki-67/MIB expressions were higher in CWR22 than PC3 xenografts. Our initial preclinical observations suggest that there may be an association between androgen signaling and thymidine metabolism and that ^{18}F-FMAU PET may be useful in prostate tumor characterization.

Keywords

^{18}F-FMAU; Prostate; Cancer; Proliferation; microPET

Introduction

Prostate cancer is the most common cancer and the second leading cause of cancer death affecting men in the United States. There is currently a lack of an accurate objective imaging-based method for the characterization (indolent vs. lethal) of the primary prostate tumor. Image-guided detection, localization, and characterization of tumor will alleviate the current major problems of the conventional “blind” biopsy approach which includes overdiagnosis (and overtreatment) of indolent tumors and underdiagnosis (and undertreatment) of aggressive prostate cancers.

Address for Correspondence and Reprints: Hossein Jadvar, MD, PhD, MPH, MBA, University of Southern California, 2250 Alcazar Street, CSC/IGM 102, Los Angeles, CA 90033, Tel: 323-442-1107, Fax: 323-442-3253, jadvar@usc.edu.

Disclosure
The radiochemistry preparation and procedures for ^{18}F-FMAU has been patented under US patent 7,273,600 B2 (Inventors: PS Conti, MM Alauddin, JD Fissekis) and the patent has been assigned to the University of Southern California (USC), Los Angeles, CA. None of the authors have any financial interest in this patent.

There is an increasing interest in the potential role of positron emission tomography (PET) in prostate cancer. Given the biological and clinical heterogeneity of prostate cancer, PET would be an ideal imaging tool for noninvasive interrogation of the underlying tumor biology in different phases of the disease. The cumulative current experience with PET and the most studied radiotracers, namely ^{18}F-fluorodeoxyglucose, ^{18}F- or ^{11}C -choline and ^{18}F- or ^{11}C -acetate suggests a generally limited role for these radiotracers in the imaging-based characterization of prostate tumor due to the overlap of uptake among normal, benign prostatic hyperplasia, and prostate cancer tissues (1). Several other promising radiotracers have been investigated in the imaging evaluation of prostate cancer including 16β-^{18}F-fluoro-5α-dihydrotestosterone (^{18}F-FDHT), targeted to the androgen receptor, anti-1-amino-3-^{18}F-fluorocyclobutane-1- carboxylic acid (anti-^{18}F-FACBC), which is a synthetic L-leucine analog, and prostate specific membrane antigen (PSMA)-based PET radiotracers (2). However, the exact diagnostic roles of these radiotracers in prostate cancer remain undefined and will require continued investigations.

The goal of our study was to determine whether imaging assessment of cellular proliferation in prostate cancer might be useful in tumor characterization. Although ^{18}F-fluorthymidine is the most studied PET radiotracer for imaging cellular proliferation in cancer, the high physiologic accumulation of this tracer in marrow and the high bladder urine activity may limit its utility in prostate cancer. On the other hand, [^{18}F]-2′-fluoro-5-methyl-1-beta-D-arabinofuranosyluracil (^{18}F-FMAU) has no or very little accumulation in bone (a common site for metastasis from prostate cancer) and in urinary bladder that renders it a potentially ideal PET radiotracer for imaging DNA synthesis in prostate cancer (3). We therefore hypothesized that ^{18}F-FMAU PET may be helpful in prostate tumor characterization for differentiating indolent from aggressive tumors with the supposition that tumors with higher tracer uptake are biologically more aggressive (e.g. higher growth rate).

^{18}F-FMAU is a thymidine analog that is phosphorylated by thymidine kinase and incorporated into the DNA (4). It was originally of clinical interest as an anticancer and an antiviral drug when used in pharmacological dose (5). In tracer doses, ^{18}F-FMAU can be useful for imaging DNA synthesis and tumor proliferation (6–10). It has also been used for imaging reporter gene expression using the herpes simplex virus type 1 thymidine kinase (HSV-tk1) system (11–14). Pharmacokinetic studies have shown that radiolabeled ^{18}F-FMAU behaves very similar to the pyrimidine nucleoside, thymidine, with respect to cellular uptake velocity, saturability of cellular incorporation, and intracellular metabolite pools and is reflective of tumor cell division (7). Initial imaging-based biodistribution of ^{18}F-FMAU in normal dogs have shown that it is resistant to degradation and is selectively retained in DNA (15).

We set out to assess the biodistribution and tumor uptake of ^{18}F-FMAU in androgen-sensitive and androgen-independent xenograft models of human prostate cancer. We also studied the potential effect of androgen on the implanted tumor uptake by using castrated and noncastrated mice to model, respectively, absence and presence of physiologic level of androgen.

Materials and Methods

^{18}F-FMAU Radiosynthesis

The radiosynthesis of ^{18}F-FMAU was performed using the newly developed one-pot labeling procedures (16). Briefly, the radiosynthesis involves radiofluorination of 2-trifluoromethanesulfonyl-1,3,5-tri-O-benzoyl ribofuranose to 2-[^{18}F]-fluoro-1,3,5-tri-Obenzoyl arabinofuranose derivative followed by the conjugation with 2,4-bis-trimethylsilyluracil in the presence of hexamethyldisilazane (HMDS) and Trimethylsilyl

Trifluoromethanesulfonate (TMSOTf). Finally, hydrolysis of the protecting groups from the sugar moiety and HPLC purification produces the desired product. ^{18}F-FMAU was obtained in 12±3% radiochemical yield with 547 mCi/μmol specific activity. The overall radiosynthesis time was about 150 min and the radiochemical purity was >99%.

Tumor Cell lines, Animals and Experimental Protocol

We employed androgen-dependent CWR22 and androgen-independent PC3 human prostate cancer cell lines (American Type Culture Collection, Manassas, VA). The androgen-dependent CWR22 human prostate cancer cell line expresses androgen receptors and PSA and is stimulated by dihydroxytestosterone. The androgen-independent PC3 human prostate cancer cell line was initiated from a bone metastasis of a grade IV prostatic adenocarcinoma and displays low testosterone-5α-reductase activity.

Surgically castrated and noncastrated mice were purchased (Harlan Sprague-Dawley, Inc., Indianapolis, IN) and served as models for the absence and presence, respectively, of androgens. No testosterone pellets or blood sampling for androgen level was employed. Tumor volume was calculated using the formula $(S^2 \times L)/2$, where S and L represent the small and large diameters of the lesion (17). The lesion dimensions were measured using calipers at every 2- to 3-day interval.

We implanted either CWR22 or PC3 human prostate cancer cells at a concentration of 5×10^6 cells per 0.1 mL in one thigh of 4- to 6-week-old, 20 to 30 g, castrated ($n = 4$) or noncastrated ($n = 6$) male athymic mice (BALB/c nu/nu), and the tumors were allowed to grow to 0.5 cm^3. Separate control non-tumor bearing athymic male mice were also included for imaging and biodistribution studies at 2h (3 castrated, 3 noncastrated) and 3h (4 castrated, 4 noncastrated) after tracer administration. Tumor cells were stained with trypan blue and viable cells were counted using a hemocytometer under a light microscope.

All animal studies were approved by our Institutional Animal Care and Use Committee, the Biological Safety Committee, and the Radiation Safety Committee. Anesthesia was induced using 2% isoflurane in oxygen and maintained throughout all imaging studies. Euthanasia was performed by cervical dislocation while the animal was anesthetized. Animals were housed in the vivarium facility during the period of tumor growth and were fed regular rodent food and water *ad libidum*.

MicroPET Imaging and Biodistribution Studies

PET scans were performed on the microPET R4 (Concorde Microsystems, Inc., Knoxville, TN) and followed by microCT imaging (InveonCT, Siemens Medical Solutions USA, Inc., Knoxville, TN) for anatomical reference. Immediately following tail vein administration of 200 μCi of ^{18}F-FMAU, dynamic PET scan was performed for 1h (4 castrated, 6 noncastrated) followed by additional 10 minute static scans at 2h and 3h time points (4 castrated, 5 noncastrated). PET data were all reconstructed using the 2D-OSEM algorithm supplied by microPET Manager (Siemens Medical Solutions USA, Inc., Knoxville, TN) into 128×128×63 images with 0.084 mm × 0.084 mm × 1.21 mm resolution. CT scans were acquired in two bed positions using the following settings: 80 kVp, 500 uA, 100 ms/180 steps covering 360 degrees and reconstructed into 768×768×923 images with 0.105 mm isotropic resolution. The dynamic PET data were histogrammed into 11 frames while static data were histogrammed into single frames using the MicroPET Manager software (Concorde Microsystems, Inc., Knoxville, TN). PET and CT images were co-registered using rigid transformations as both scans were performed using warmed multi-modality imaging chambers and animals were not moved between scans. Immediately following microPET imaging, animals were sacrificed for biodistribution studies. Blood, tumor and

organs were harvested, weighed and counted for radioactivity on a Packard Cobra II Gamma Counter (Packard Instruments, Inc., Meriden, CT).

Immunohistochemical Assays

Xenograft tumor tissue samples were fixed in 4% freshly prepared buffered paraformaldehyde, embedded in paraffin according to standard histologic protocols and sectioned at a thickness of 5 μm. Routine histologic staining with hematoxylin-eosin and immunohistochemical assays for cellular proliferation parameter, Ki-67/MIB, and androgen receptor were performed to obtain qualitative appraisal on the magnitudes of their expression in the implanted prostate tumors.

Data Analysis and Statistics

Tissue tracer uptake was calculated as standardized uptake value (SUV) from the PET data and as percent injected dose/gram of tissue (%ID/g) from the biodistribution data and expressed as ratios to the activities of muscle, blood, or liver. Two-group comparisons of data were performed between tumor types in a particular animal type and between animal types for a particular tumor type using a two-tailed Student *t*-test with unequal variance and with a significance probability level of less than 0.05.

Results

Biodistribution Studies

Control biodistribution studies in non-tumor bearing mice demonstrated significantly higher ^{18}F-FMAU uptake in all major organs of castrated animals in comparison to noncastrated animals suggestive of generalized tracer retention in the castrated animal (Table 1). Similar observation was noted with the tumor bearing mice biodistribution studies. Figure 1 shows biodistribution studies that were performed at 3h after tracer administration in mice bearing either CWR22 or PC3 implanted xenografts. It is clear that there was consistently higher tracer uptake in the all major organs as well as in the implanted tumors in the castrated animals when compared to those in noncastrated mice. In both animal types, the organs with the highest tracer uptake were the liver, spleen, and kidneys. Bowel showed variable but generally high uptake. Bone uptake level was low and similar to muscle reference (noncastrated: 1.63±0.86 vs.1.57±0.95 %ID/g; castrated: 3.27±1.19 vs. 3.01±1.38 %ID/g, respectively; all values at 3h)

MicroPET Studies

In the tumor-bearing animals, visually there was high tracer uptake in both tumor types implanted in either animal type. The dynamic microPET demonstrated a representative uptake profile for the tumors that increased relatively rapidly to a plateau (within about 10 minutes after tracer administration) at which point the uptake level increased slowly. Conversely, uptake in the reference tissues of muscle and liver showed rapid decline in uptake particularly at about 1h such that by 3h post tracer administration, the tumor uptake was substantially higher than the uptake levels in the liver (by an average factor of 1.45) and the muscle (by an average factor of 2.28)(Figure 2). The organs with the highest tracer accumulation on microPET were the same as those noted on the biodistribution studies (i.e. liver, spleen, kidneys). Also the excreted tracer progressively accumulated in the urinary bladder.

Effect of Tumor and Animal Type

For androgen-dependent CWR22 xenografts, when compared to castrated animal, the noncastrated animal showed significantly higher tumor-to-liver (1.72±0.12 vs. 1.3±0.17,

p=0.003) and tumor-to-blood (2.93±0.21 vs. 2.32±0.13, p=0.001) uptake ratios at 3h. Conversely for androgen-independent PC3 xenografts, no statistically significant difference was seen in the tumor-to-non-proliferating tissue reference (either muscle or liver) uptake ratios between the castrated and the noncastrated animals. Moreover, when compared to PC3 tumors, CWR22 xenografts showed significantly higher tumor-to-muscle (2.56±0.30 vs. 1.99±0.30, p=0.008) and tumor-to-liver uptake ratios (1.72±0.12 vs. 1.26±0.17, p=0.0003) but this was only observed in the noncastrated animal and at the 3h time period (Figure 3).

Qualitative Assessment of Immunohistochemical Assays

Histological assessment demonstrated few small areas of necrosis in the harvested tumors. Qualitative visual assessment of the immunohistochemical assays showed higher expressions of both androgen receptor and Ki-67/MIB in the CWR22 xenograft when compared to the implanted PC3 tumor (Figure 4).

Discussion

The standard transrectal ultrasound guided 10–12 core prostate biopsy misses about 38% of tumors due to multifocal distribution of prostate cancer (18). Using this procedure, even when prostate cancer is diagnosed, the possible co-existent high grade tumor may be missed leading to underdiagnosis of these tumors and subsequent therapy failures. Saturation (>20) biopsy procedures cannot compensate for the shortcoming of blind conventional biopsy procedure since it leads to overdiagnosis and overtreatment of clinically insignificant tumors at substantial morbidity to the individual patient and financial cost to the healthcare system (19). Therefore there is a critical need for image-guided biopsy that optimizes the probability of detection of biologically and clinically relevant tumors (e.g. aggressive tumors) and reduces the biopsy rate of clinically insignificant tumors. Image-guided characterization will also pave the way for rational treatment decision-making including active surveillance for low grade tumors and focal therapy (male lumpectomy) for localized aggressive tumors.

We therefore set out to assess the potential utility of the cellular proliferation imaging marker, ^{18}F-FMAU, in preclinical xenograft model of human prostate cancer. It is prudent to presume that biologically more aggressive prostate tumors would display higher cellular proliferative phenotype. A number of PET-based proliferation tracers have been explored, typically in conjunction with tracers for the thymidine salvage pathway of DNA synthesis (20). The most studied thymidine analog has been ^{18}F-fluorothymidine (FLT). FLT is phosphorylated by thymidine kinase 1, incorporated by the normal proliferating marrow and glucuronidated in the liver. Experience with ^{18}F-FLT in prostate cancer is very limited although recently in preclinical models of castrate-resistant prostate cancer, this tracer has been shown to be potentially useful for monitoring response to docetaxel treatment (21). However, the physiologic high marrow accumulation of ^{18}F-FLT severely limits its clinical utility in detection and assessment of treatment response in bone metastases.

On the other hand, ^{18}F-FMAU is incorporated to DNA after phosphorylation and shows substantially less marrow uptake which is a useful feature for imaging assessment of prostate cancer. Our biodistribution studies showed relatively high uptake in the normal heart, kidneys, and liver, similar to prior studies, which is thought to be related in part to the role of mitochondrial thymidine kinase 2 (4). We also observed high steady tracer accumulation in the xenograft human prostate cancer tumors. High activity was noted in the urinary bladder in relation to accumulating excreted tracer. Interestingly prior studies have shown relatively low ^{18}F-FMAU accumulation in the dog urinary bladder (15). This may be due species differences and will need further investigation in humans. Our results are also in

line with those of prior studies in that bone uptake level is low which renders ^{18}F-FMAU useful for the imaging evaluation of osseous metastases of prostate cancer (3).

We found that despite some decay in radioactivity, delayed imaging at 3h post tracer administration might be needed for improved tumor-to-reference tissue uptake ratio which was essentially related to steady general decline in the background activity in the setting of plateau or slowly increasing tumor uptake. In fact at 3h, we observed a statistically significant difference in the tumor-to-reference tissue (either liver or muscle) uptake ratios between the two tumor types in the noncastrated mice. The higher ^{18}F-FMAU uptake in the CWR22 tumor appeared to be associated with the relatively strong expression of the cellular proliferation index Ki-67/MIB. As expected, the androgen receptor expression level was higher in the CWR22 xenograft than the PC3 tumor. When identical experiments were performed in the castrated mice, such difference between the tumor-to-reference uptake ratios for the two tumor types was not observed. Biodistribution studies revealed that this finding was largely due to the generally higher tracer retention in the castrated animal, thereby reducing the tumor-to-reference tissue uptake ratios even at 3h after tracer administration. Another contributing factor may be the reduction in cellular proliferation of the androgen-dependent tumor after androgen withdrawal (22, 23).

The exact biological mechanism for the apparent generalized ^{18}F-FMAU retention in the castrated mouse and the relationship of this observed phenomenon to the absence of androgen are unknown. We did not measure the plasma level of androgen in the noncastrated mice and relied on the intrinsic androgen level in the noncastrated mice to model and maintain the physiologic condition. The observation of generalized organ ^{18}F-FMAU retention in the absence of androgen was an interesting finding. Although beyond the scope of the current report and our initial experimental design, we plan to perform follow-up longitudinal test-retest biodistribution and imaging studies utilizing non-tumor bearing castrated mice before and after subcutaneous implantation of a time release testosterone pellet which will enable us to assess the effect of androgen on ^{18}F-FMAU biodistribution within the same animal. Additional imaging after systemic clearance of testosterone (~2–4 weeks after pellet implantation) allows confirmation of our current preliminary observation of a possible association between androgen and physiologic ^{18}F-FMAU biodistribution upon which additional biochemical investigations may be necessary to elucidate the exact mechanistic association between androgen signaling and thymidine metabolism. One possibility may be the androgen control of mitochondrial function that may include thymidine kinase 2 enzymatic activity (24)

Our study should be interpreted in the context of preclinical subcutaneous xenograft model that was employed. Generally, factors such as tumor microvasculature, oxygenation distribution, and differences in the growth pattern and tumor microenvironment may limit extrapolation from tumor models in animals to the native spontaneous tumors in humans (25). Despite this broad limitation in extending results from animal models to the human condition, xenograft tumor models are commonplace in the preclinical studies.

In summary, our preliminary observation with ^{18}F-FMAU in prostate cancer xenografts suggests that there may be a role for ^{18}F-FMAU in image-based characterization of tumor in the noncastrate state when men present at the time of initial evaluation for prostate cancer. Moreover, ^{18}F-FMAU uptake in the androgen-dependent prostate tumor may be sensitive in responding to the differences in circulating androgen levels and as such may provide useful imaging-based information on impending castrate-resistant state. Additional preclinical work in other prostate cancer cell lines and spontaneous tumors in mice as well as pilot human studies will be needed to decipher the exact role of ^{18}F-FMAU in the imaging evaluation of prostate cancer.

Acknowledgments

This work was supported by the National Institutes of Health, National Cancer Institute Grant number R21-CA142426 (H. Jadvar). We thank Fatemeh Abdollahi Mofakham and Aida Kouhi for their help with the animal procedures.

References

1. Jadvar H. Prostate cancer: PET with ^{18}F-FDG, ^{18}F- or ^{11}C-acetate, and ^{18}F- or ^{11}C-choline. J Nucl Med. 2010; 52:81–89. [PubMed: 21149473]
2. Apolo AB, Pandit-Taskar N, Morris MJ. Novel tracers and their development for the imaging of metastatic prostate cancer. J Nucl Med. 2008; 49:2031–41. [PubMed: 18997047]
3. Shields AF. Positron emission tomography measurement of tumor metabolism and growth: its expanding role in oncology. Mol Imaging Biol. 2006; 8:141–50. [PubMed: 16534552]
4. Tehrani OS, Douglas KA, Lawhom-Crews JM, et al. Tracking cellular stress with labeled FMAU reflects changes in mitochondrial TK2. Eur J Nucl Med Mol Imaging. 2008; 35:1480–8. [PubMed: 18265975]
5. Fanucchi MP, Leyland-Jones R, Young CW, et al. Phase I trial of 1-(2′-deoxy-2′-fluoro-1-beta-Darabinofuranosyl)-5-methyluracil (FMAU). Cancer Treat Rep. 1985; 69:55–9. [PubMed: 2981621]
6. Conti PS, Alauddin MM, Fissekis JR, et al. Synthesis of 2′-fluoro-5-[11C]-methyl-1-beta-Darabinofurasyluracil ([11C]-FMAU): a potential nucleoside analog for in vivo study of cellular proliferation with PET. Nucl Med Biol. 1995; 22:783–9. [PubMed: 8535339]
7. Bading JR, Shahinian AH, Bathija P, et al. Pharmacokinetics of the thymidine analog 2′-fluoro-5-[(14)C]-methyl-1-beat-D-arabinofuranosyluracil ([(14)C]FMAU in rat prostate tumor cell. Nucl Med Biol. 2000; 27:361–8. [PubMed: 10938471]
8. Wang H, Oliver P, Nan L, et al. Radiolabeled 2′-fluorodeoxyuracil-beat-D-arabinofuranoside (FAU) and 2′-fluoro-5-methyldeoxyuracil-beta-D-arabinofuranoside (FMAU) as tumor imaging agents in mice. Cancer Chemother Pharmacol. 2002; 49:419–24. [PubMed: 11976837]
9. Lu L, Samuelsson L, Bergstrom M, et al. Rat studies comparing 11C-FMAU, 18F-FLT, and 76Br-BFU as proliferation markers. J Nucl Med. 2002; 43:1688–98. [PubMed: 12468521]
10. Mangner TJ, Klecker RW, Anderson L, et al. Synthesis of 2′-deoxy-2′-[18F]fluoro-beta-D-arabinofuranosyl nucleosides, [18F]FAU, [18F]FMAU, [18F]FBAU and [18F]FIAU, as potential PET agents for imaging cellular proliferation. Synthesis of [18F] labeled FAU, FMAU, FBAU, FIAU. Nucl Med Biol. 2003; 30(3):215–24. [PubMed: 12745012]
11. de Vries EF, van Waarde A, Harmsen MC, et al. [(11)C]FMAU and [(18)F]FHPG as PET tracers for herpes simplex virus thymidine kinase activity and human cytomegalovirus infections. Nucl Med Biol. 2000; 27:113–9. [PubMed: 10773539]
12. Alauddin MM, Shahinian A, Gordon EM, et al. Evaluation of 2′-deoxy-2′-fluoro-5-methyl-1-beta-Darabinofurasyluracil as a potential gene imaging agent for HSV-tk expression in vivo. Mol Imaging. 2002; 1:74–81. [PubMed: 12920847]
13. Alauddin MM, Shahinian A, Gordon EM, et al. Direct comparison of radiolabeled probes FMAU, FHBG, and FHPG as PET imaging agents for HSV1-tk expression in a human breast cancer model. Mol Imaging. 2004; 3:76–84. [PubMed: 15296672]
14. Kang KW, Min JJ, Chen X, et al. Comparison of [14C]FMAU, [3H]FEAU, [14C]FIAU, and [3H]PCV for monitoring reporter gene expression of wild type and mutant herpes simplex virus type I thymidine kinase in cell culture. Mol Imaging Biol. 2005; 7:296–303. [PubMed: 16041591]
15. Sun H, Mangner TJ, Collins JM, et al. Imaging DNA synthesis in vivo with 18F-FMAU and PET. J Nucl Med. 2005; 46(2):292–6. [PubMed: 15695789]
16. Li Z, Cai H, Conti PS. Automated synthesis of 2′-deoxy-2′-[18F]fluoro-5-methyl-1-β-D-arabinofuranosyluracil ([18F]-FMAU) using a one reactor radiosynthesis module. Nucl Med Biol. 2011; 38(2):201–6. [PubMed: 21315275]
17. Price DT, Coleman RE, Liao R, et al. Comparison of [18F]fluorocholine and [18F]fluorodeoxyglucose for positron emission tomography of androgen dependent and androgen independent prostate cancer. J Urol. 2002 Jul; 168(1):273–80. [PubMed: 12050555]

18. Patel A, Jones J, Rabets J, et al. Parasagittal biopsies add minimal information in repeat saturation prostate biopsy. Urology. 2004; 63:87–9. [PubMed: 14751355]

19. Stav K, Liebovici D, Sandbank J, et al. Saturation prostate biopsy in high risk patients after multiple previous negative biopsies. Urology. 2008; 71:399, 403. [PubMed: 18342172]

20. Bading JR, Shields A. Imaging of cell proliferation: status and prospects. J Nucl Med. 2008; 49:64S–80S. [PubMed: 18523066]

21. Oyama N, Hasegawa Y, Kiyono Y. Early response assessment in prostate carcinoma by 18F-fluorothymidine following anticancer therapy with docetaxel using preclinical tumor models. Eur J Nucl Med Mol Imaging. 2011; 38:81–9. [PubMed: 20878403]

22. Agus DB, Cordon-Cardo C, Fox W, Drobnjak M, et al. Prostate cancer cell cycle regulators: response to androgen withdrawal and development of androgen independence. J Natl Cancer Inst. 1999; 91:1869–76. [PubMed: 10547394]

23. Kim D, Gregory CW, French FS, et al. Androgen receptor expression and cellular proliferation during transition from androgen-dependent to recurrent growth after castration in CWR22 prostate xenograft. Am J Path. 160:219–226. [PubMed: 11786415]

24. Doeg KA, Polomski LL, Doeg LH. Androgen control of mitochondrial and nuclear DNA synthesis in male sex accessory tissue of castrate rats. Endocrinology. 1972; 90:1633–8. [PubMed: 5020313]

25. Pienta KJ, Abate-Shen C, Agus DB, et al. The current state of preclinical prostate cancer animal models. Prostate. 2008; 68:629–639. [PubMed: 18213636]

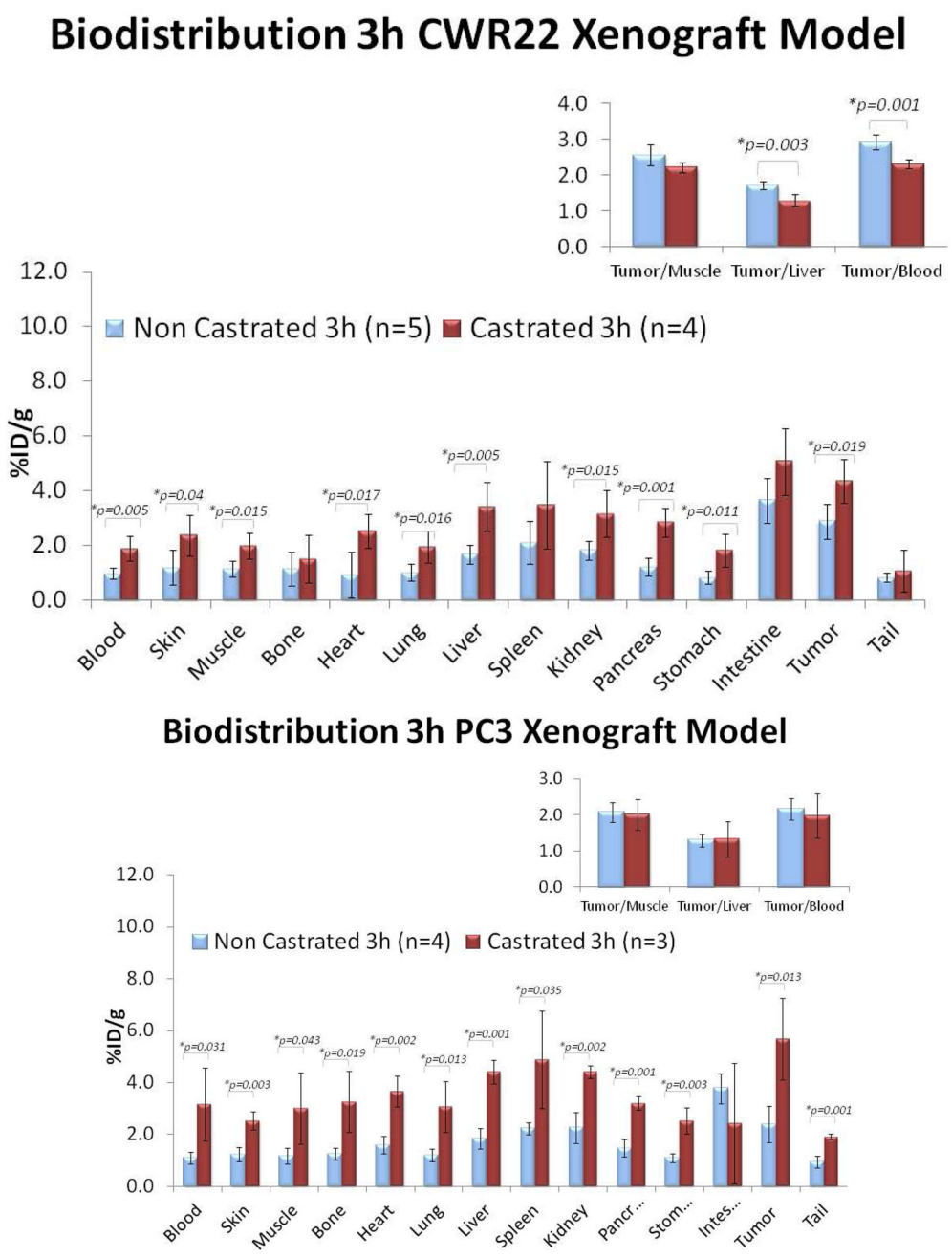

Figure 1.

Biodistribution of ^{18}F-FMAU at 3h after tail vein administration in athymic castrated (red bars) and noncastrated (blue bars) male mice bearing either (a) CWR22 or (b) PC3 implanted human prostate cancer xenografts. In both animals, the organs with the highest tracer uptake were the liver, spleen, and kidneys. Note the generalized organ tracer retention in the castrated mice. The CWR22 tumor-to-liver and tumor-to-blood uptake ratios were significantly higher in the noncastrated animal.

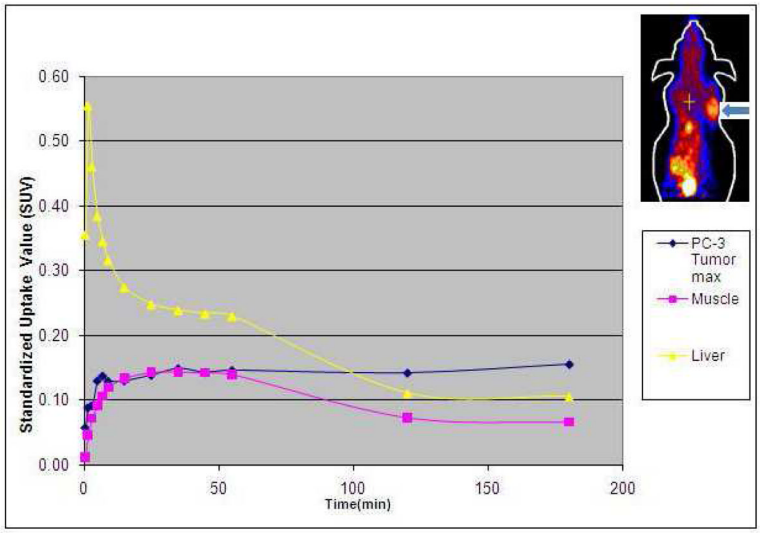

Figure 2.

Representative 3h duration time-activity curves obtained from regions of interest placed over PC3 tumor (arrow on mouse image in top right corner), liver and muscle on dynamic microPET images. Note the early rapid decline in the hepatic activity with a steady decline in both the liver and muscle uptake levels after one hour. The tumor uptake level rises rapidly reaching a plateau with continued slow rise. After 2h, the tumor uptake level is higher than the uptake levels in the liver and the muscle.

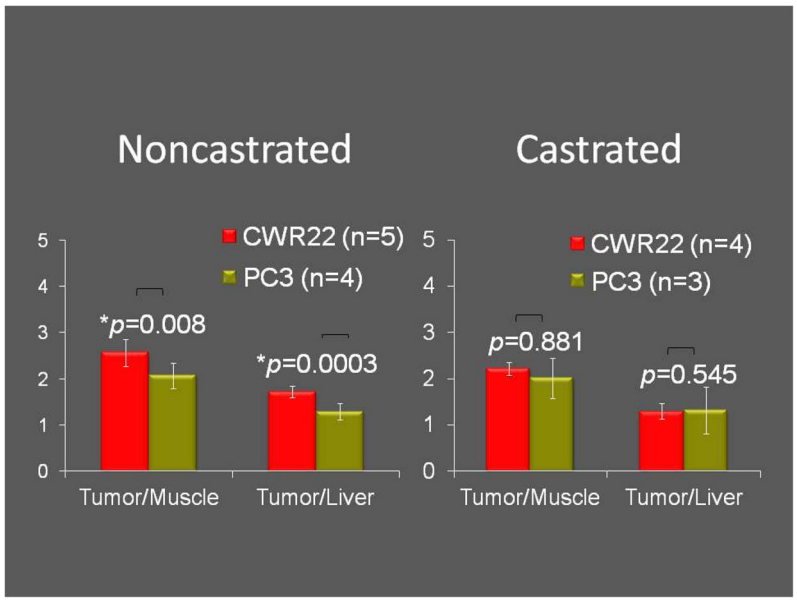

Figure 3.
^{18}F-FMAU uptake levels in the two tumor types (CWR22: left bars, PC3: right bars) were significantly different only in the noncastrated animal at the 3h time point.

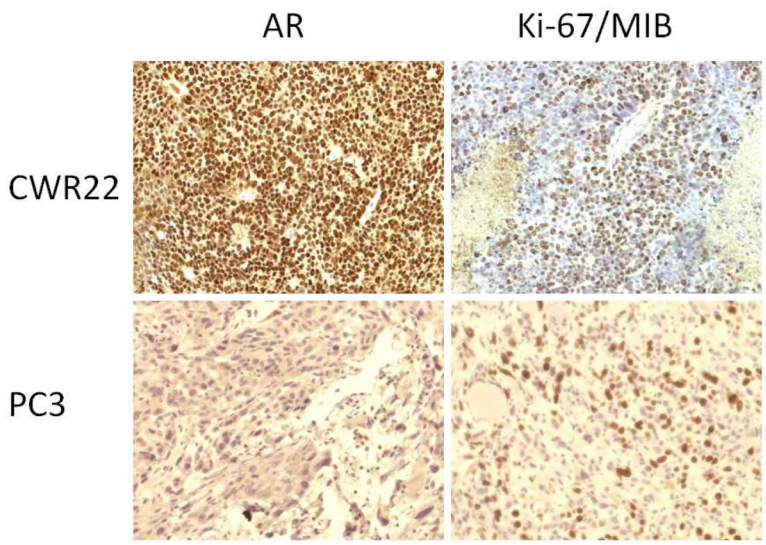

Figure 4.
Immunohistochemical stains (left: androgen receptor, AR; right: cellular proliferation index, Ki-67/MIB) for CWR22 (top panel) and PC3 (bottom panel) implanted tumors (objective magnification × 20). Note the relatively strong expression of AR and Ki-67/MIB in the CWR22 tumor tissue in comparison to those of the PC3 tumor tissue.

Mol Imaging. Author manuscript; available in PMC 2012 September 14.

Table 1

Biodistribution of ^{18}F-FMAU in major organs of control non-tumor-bearing noncastrated and castrated mice at 2h and 3h. The p-values at 2h and 3h refer to comparison of the corresponding tissue mean uptake levels in the noncastrated and the castrated animals. All comparisons were statistically significant except for the 2h time point renal and bowel uptake levels. Note the generalized tissue tracer retention in the castrated animal in comparison to the noncastrated animal.

%ID/g (mean+S.E.)	Noncastrated		Castrated		p-value (2h)	p-value (3h)
	2h (n=3)	3h (n=4)	2h (n=3)	3h (n=4)		
Blood	1.62±0.11	0.16±0.03	2.75±0.38	0.51±0.09	0.008	0.002
Muscle	1.86±0.08	0.23±0.07	3.10±0.28	0.59±0.06	0.002	0.002
Liver	3.09±0.26	0.29±0.02	4.31±0.18	0.82±0.10	0.003	0.007
Spleen	2.80±0.09	0.60±0.19	4.57±0.63	1.43±0.26	0.008	0.001
Kidney	1.95±1.7	0.33±0.06	4.61±0.39	0.86±0.21	0.058	0.001
Heart	2.31±0.19	0.21±0.03	3.56±0.39	0.66±0.07	0.007	0.001
Bowel	5.43±0.12	1.64±0.62	6.55±1.22	2.38±0.13	0.189	0.045
Bone	1.77±0.14	0.44±0.29	2.87±0.07	0.74±0.13	0.001	0.037